

# Real-time Holistic Robot Pose Estimation with Unknown States

Shikun Ban<sup>1</sup> Juling Fan<sup>1</sup> Wentao Zhu<sup>1</sup> Xiaoxuan Ma<sup>1</sup> Yu Qiao<sup>2</sup> Yizhou Wang<sup>1</sup>

<sup>1</sup> Peking University <sup>2</sup> Shanghai Jiao Tong University

{bansk, julyfan}@stu.pku.edu.cn, {wtzhu, maxiaoxuan, yizhou.wang}@pku.edu.cn, qiaoyu@sjtu.edu.cn

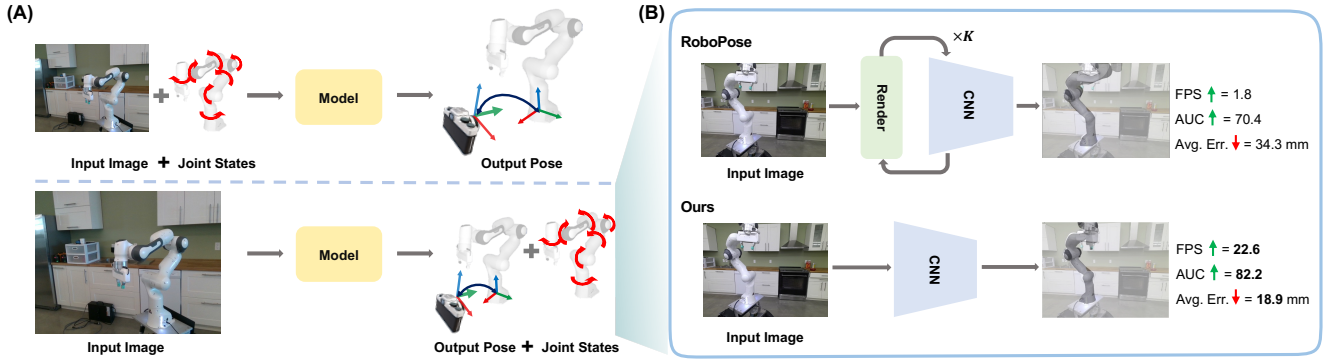


Figure 1. (A) The majority of previous works assume known robot joint states and focus solely on estimating the camera-to-robot pose, *i.e.* camera-to-robot rotation and translation. In contrast, the holistic robot pose estimation problem requires estimating both joint states and the camera-to-robot pose, given only an RGB image without known joint states. (B) For holistic robot pose estimation, RoboPose [14] uses costly test-time optimization to iteratively refine the predictions. In contrast, our feed-forward method achieves state-of-the-art accuracy with a  $12\times$  speed boost.

## Abstract

Estimating robot pose from RGB images is a crucial problem in computer vision and robotics. While previous methods have achieved promising performance, most of them presume full knowledge of robot internal states, *e.g.* ground-truth robot joint angles, which are not always available in real-world scenarios. On the other hand, existing approaches that estimate robot pose without joint state priors suffer from heavy computation burdens and thus cannot support real-time applications. This work addresses the urgent need for efficient robot pose estimation with unknown states. We propose an end-to-end pipeline for real-time, holistic robot pose estimation from a single RGB image, even in the absence of known robot states. Our method decomposes the problem into estimating camera-to-robot rotation, robot state parameters, keypoint locations, and root depth. We further design a corresponding neural network module for each task. This approach allows for learning multi-facet representations and facilitates sim-to-real transfer through self-supervised learn-

ing. Notably, our method achieves inference with a single feedforward, eliminating the need for costly test-time iterative optimization. As a result, it delivers a  $12\times$  speed boost with state-of-the-art accuracy, enabling real-time holistic robot pose estimation for the first time. Code is available at <https://oliverbansk.github.io/Holistic-Robot-Pose/>.

## 1. Introduction

Robot pose estimation is a fundamental task in computer vision and robotics as it not only lays the groundwork for multiple downstream tasks, *e.g.* visually-guided object grasping and manipulation [20, 35, 41], but also paves the way for a variety of applications, such as autonomous navigation [1, 12, 30, 31], human-robot interaction [3, 34, 36, 37, 39] and multi-robot collaboration [19, 27, 38]. Nonetheless, most previous works for monocular robot pose estimation [15, 17, 21, 35] rely on a known set of robot joint angles as an additional input to alleviate the difficulty of the estimation process. However, this prerequisite informa-

tion of the robot state is not always available in practical scenarios. For instance, low-cost robotic arms without sophisticated sensors or internal monitors can not provide the visual calibration process with readily accessible robot state measurements [4, 10, 41]. Moreover, in the context of collaborative robotics, the reliability of the state information from the counterpart robot is not always warranted as trust issues between robotic systems potentially arise [11, 13], further posing a pressing demand for monocular robot pose estimation with unknown robot joint state at test time.

In this work, we address the challenge of *Holistic Robot Pose Estimation* with unknown internal states for articulated robots. Specifically, given a monocular RGB image, we aim to simultaneously solve for 6D robot pose (3D rotation and translation relative to the camera) and fine-grained robot joint state parameters (including joint angles for revolute joints and displacement for prismatic joints).

Nonetheless, learning holistic robot pose estimation without joint state information presents significant challenges. The primary challenge is the dual ambiguities resulting from the simultaneous unknowns of joint state and 6D pose. Specifically, estimating the 6D pose for an articulated robot presents greater complexity compared to a rigid object, due to the variability in shape and scale introduced by the unknown joint states. On the other hand, the task of estimating joint states requires establishing 2D-to-3D correspondences, a process further complicated by the concurrent unknowns in the 6D pose. This intertwined challenge calls for novel solutions capable of decoupling the joint and the 6D pose from each other. Furthermore, the sophisticated robot morphologies vary from model to model, requiring non-trivial model design. In addition, The robot parts are frequently invisible in the monocular image as a result of self-occlusion and truncation, posing more challenges for robust estimation. Finally, the domain gap between synthetic training data and real-world images introduces additional challenges for learning-based approaches.

It is worth noting that some previous works [14, 41] have also explored the setting of holistic estimation with unknown states, and addressed some of the challenges. However, these methods all necessitate iterative optimization at inference, which is computation-intensive and unable to support real-time applications. Motivated by the need for efficient holistic robot pose estimation without knowledge of the robot state, we propose an end-to-end framework that directly estimates camera-to-robot pose and robot joint state parameters, requiring only a single feed-forward pass during inference.

In pursuit of this goal, we factorize the holistic robot pose estimation task into several sub-tasks, including the estimation of camera-to-robot rotation, robot joint states, root depth, and root-relative keypoint locations. We then design corresponding neural network modules for each sub-task. Specifically, the standalone root depth estimator disentangles

the estimation of scale-variant and scale-invariant variables. The keypoint estimator bridges the gap between the pixel space and the robotic parameter space. Additionally, we utilize self-supervised consistency regularizations which could be performed on the real images without ground truth (GT).

We demonstrate that our designs of modular feed-forward networks improve model generalization while maintaining high computation efficiency. Consequently, our approach achieves state-of-the-art estimation accuracy with unknown robot states and a  $12\times$  speedup compared to the iterative Render-and-Compare (RnC) [14] approach, as depicted in Fig. 1. The key insight behind our approach is that we could get rid of the cumbersome RnC [14] and error-prone Perspective-n-Points (PnP) [17, 21, 35] schemes to establish 2D-3D correspondences. Instead, we demonstrate that feed-forward networks could well handle the problem with proper problem decomposition and meticulous design.

In summary, our contributions are three-fold:

1. We present an efficient end-to-end learning framework for the holistic robot pose estimation problem with unknown robot states.
2. We propose to factorize the holistic robot pose estimation problem into several sub-tasks and tackle them with respective modules.
3. We achieve state-of-the-art performance on various robot models while delivering a significant  $12\times$  speedup, paving the way for real-time applications.

## 2. Related Work

### 2.1. Hand-eye calibration

The goal of Hand-Eye Calibration (HEC) is to determine the transformation between the position of a robot’s end-effector (hand) and its vision system (eye). This task can be categorized into two types: *eye-in-hand* where the camera is fixed at the robot end-effector [25], and *eye-to-hand* which refers to the configurations where the camera is placed at a distance from the robot [5, 22, 28]. This work focuses on a similar setting with eye-to-hand. Traditional HEC methods involve attaching a fiducial marker to the end effector [6, 7, 26], placing it in several known positions, detecting the marker positions in images, and then solving for the camera-to-robot transformation. Despite its broad applicability, the classical HEC pipeline necessitates a complete offline calibration process every time the camera-robot transformation changes, which can be tedious in real-world applications. Consequently, recent works, such as DREAM [17], propose an online, markerless calibration problem, as discussed below.

### 2.2. Image-based robot pose estimation

Previous works can be divided into two categories based on whether the robot states are known or not. Most previous works estimate the 6D camera-to-robot pose with

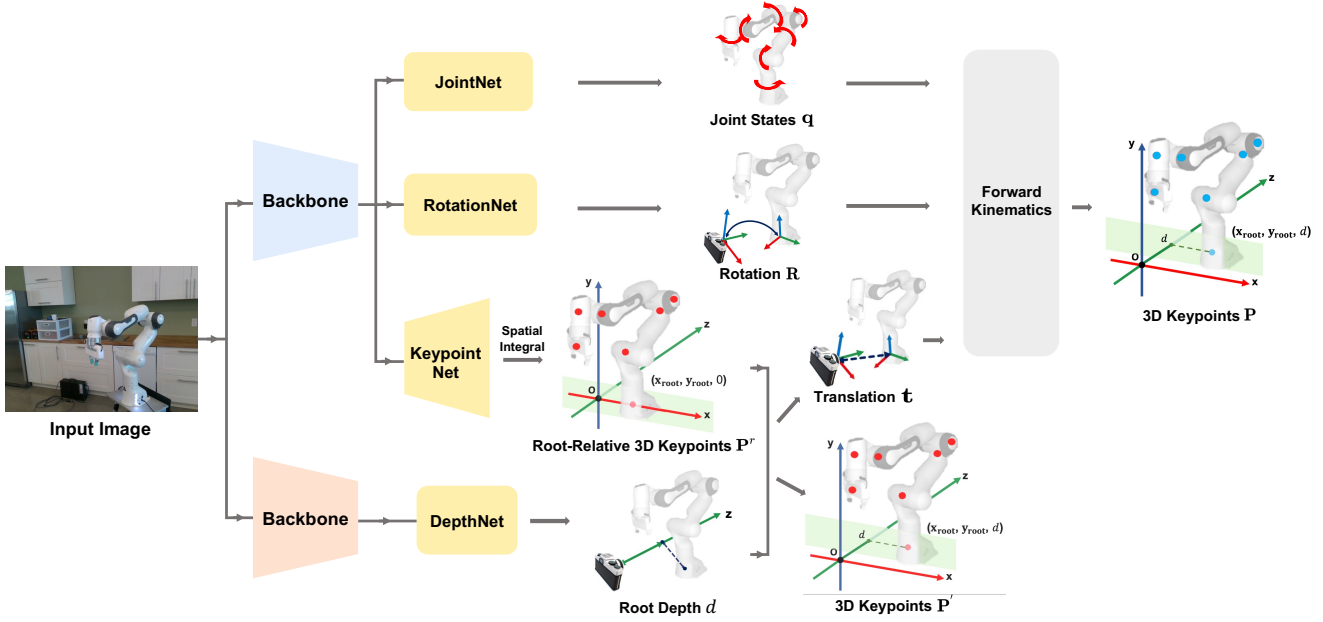


Figure 2. Framework overview. The *JointNet* and the *RotationNet* regress joint state parameters  $\mathbf{q}$  and camera-to-robot rotation  $\mathbf{R}$ , respectively. The *KeypointNet* estimates root-relative 3D keypoint locations  $\mathbf{P}^r$ . The *DepthNet*'s estimation of root depth  $d$  is combined with  $\mathbf{P}^r$  to acquire absolute 3D keypoint locations  $\mathbf{P}'$  and camera-to-robot translation  $\mathbf{t}$ . Joint state parameters  $\mathbf{q}$ , rotation  $\mathbf{R}$  and translation  $\mathbf{t}$  are used to compute 3D keypoint locations  $\mathbf{P}$  via forward-kinematics.

known robot states. For example, DREAM [17] first trains a 2D keypoint estimator and then applies Perspective- $n$ -Point (PnP) [18] to obtain camera-to-robot pose, showing comparable results with the classical methods. Some work further utilizes segmentation masks and edges to aid pose estimation [8, 16]. Chen *et al.* [2] apply rendering-based camera pose optimization and consistency-based joint space exploration. SGTAPose [35] leverages robot structure prior and temporal information. Lu *et al.* [21] propose to train on real-world data using foreground segmentation and differentiable rendering in a self-supervised manner.

Recently, several works have shifted to estimating robot pose with unknown joint states. Zuo *et al.* [41] estimate the robot pose and joint angles of a simple 4-DoF robotic arm from a single RGB image by solving a nonlinear nonconvex optimization problem. However, this method is not well-suited for robot arms with higher complexity. Labbé *et al.* [14] propose a render-and-compare approach to iteratively refine the estimation for both known and unknown states, and apply the method to different robot models up to 15-DoF. However, the iterative optimization process limits its applications in real-time scenarios. In contrast, our approach can be deployed with a single feed-forward at inference and achieves real-time efficiency.

### 3. Method

#### 3.1. Overview

Given an RGB image  $\mathbf{I}$ , we employ a suite of neural network modules, including *DepthNet*, *JointNet*, *RotationNet*, and *KeypointNet*. These modules are used to respectively estimate the absolute root depth  $d$ , joint state parameters  $\mathbf{q}$ , camera-to-robot rotation  $\mathbf{R} \in SO(3)$ , and root-relative 3D keypoint locations  $\mathbf{P}^r \in \mathbb{R}^{N \times 3}$ , where  $N$  represents the total number of keypoints. The keypoints are defined at the joint articulations, in line with previous works [14, 17, 21], and one keypoint is designated as the robot root. The root joint is critical for computing the camera-to-robot rotation  $\mathbf{R}$  and translation  $\mathbf{t}$ , as well as serving as the origin for the forward kinematics (FK) process.

Our modularized design offers several key insights. Firstly, *DepthNet* is tailored to learn the scale-variant camera-robot spatial relationship, while the other modules concentrate on the scale-invariant robot features. Secondly, while the joint state parameters  $\mathbf{q}$  provide a compact representation of robot morphologies subject to robotic structure constraints, they are highly abstract and thus challenging to directly regress from image features. To address this, we utilize the 3D keypoint locations as an intermediary. On the one hand, they can be effectively estimated with pixel-aligned image features; on the other hand, they are inherently linked to  $\mathbf{q}$  through an FK process.

An overview of the proposed framework is illustrated in Fig. 2. Specifically, *DepthNet* estimates the absolute root depth  $d$ , which, in conjunction with *KeypointNet*'s output  $\mathbf{P}^r \in \mathbb{R}^{N \times 3}$ , provides the absolute 3D keypoint locations  $\mathbf{P}' \in \mathbb{R}^{N \times 3}$ .  $\mathbf{P}'$  positions the root joint in the camera coordinates and includes the camera-to-robot translation  $\mathbf{t}$ . The estimated joint state parameters  $\mathbf{q}$ , along with the camera-to-robot rotation  $\mathbf{R}$  and translation  $\mathbf{t}$ , are then used to perform FK, yielding the final 3D keypoint estimations  $\mathbf{P} \in \mathbb{R}^{N \times 3}$ .

In the following, we will first introduce the architecture design of the network modules in Sec. 3.2, and then explain the training loss design consisting of ground-truth supervision and self-supervision in Sec. 3.3.

### 3.2. Architecture

**DepthNet.** Monocular object depth estimation suffers from significant ambiguities, as the absolute depth value and camera intrinsics are deeply intertwined [23]. For instance, a robot in a fixed pose relative to the camera may appear larger in photos taken with cameras having larger focal lengths. Scaling both the absolute depth and focal lengths equally results in identical object size and appearance in different images. To address this challenge, we implement *DepthNet* following the approach in [24] to disentangle depth from camera intrinsics.

Initially, we use camera intrinsics to calculate a normalized, coarse depth value  $d_c$ :

$$d_c = \sqrt{\frac{f_x \cdot f_y \cdot A_{real}}{A_{bbox}}}, \quad (1)$$

where  $f_x$  and  $f_y$  represent the focal lengths along the x- and y-axes,  $A_{real}$  is the area of the robot in real space (in  $mm^2$ ), and  $A_{bbox}$  is the area of the robot's bounding box (in  $pixel^2$ ). This method of calculating  $d_c$  normalizes it in 3D space and provides an approximate depth estimation for subsequent refinement.

The primary function of *DepthNet* is to predict a correction factor  $\lambda$  based on the input image. We multiply the estimated  $\lambda$  by  $d_c$  to obtain the final absolute root depth  $d$ :

$$d = \lambda \cdot d_c. \quad (2)$$

With a fixed camera, the relationship between the normalized coarse depth  $d_c$  and the robot's size in the image is linear. However, robots can assume poses with the same depth but different sizes in the image, making  $d_c$  inadequate for accurate root depth representation. The correction factor  $\lambda$  introduces non-linear flexibility to the depth estimation, addressing this issue by adjusting  $d_c$  based on image features.

**JointNet.** The goal of *JointNet* is to estimate joint state parameters  $\mathbf{q} = (q_1, q_2, \dots, q_J)$ , where  $J$  denotes the number of robot joints. Since this work deals with 1-DoF joints (revolute and prismatic),  $J$  also equals the robot's DoF. *JointNet* shares the same feature extractor with *RotationNet* and *KeypointNet*. We extract feature map  $\mathbf{F} \in \mathbb{R}^{C \times H \times W}$  (where  $C$  denotes the number of channels, and  $H \times W$  denotes the spatial resolution) and use global average pooling to obtain  $\mathbf{f} \in \mathbb{R}^C$ . Finally, we employ several MLP blocks to regress the joint state parameters  $\mathbf{q}$  from  $\mathbf{f}$ .

**RotationNet.** The goal of *RotationNet* is to estimate the camera-to-robot rotation  $\mathbf{R} \in SO(3)$ . We employ an MLP to estimate  $\mathbf{R}$  from the image feature  $\mathbf{f}$ . In practice, we utilize the 6D continuous rotation representation [40] to parameterize  $\mathbf{R}$ .

**KeypointNet.** The goal of *KeypointNet* is to estimate root-relative 3D keypoint locations  $\mathbf{P}^r \in \mathbb{R}^{N \times 3}$  for  $N$  robot keypoints. We transform the feature map  $\mathbf{F}$  to a 3D heatmap  $\mathbf{H} \in \mathbb{R}^{N \times D \times H' \times W'}$  through convolutional layers, where  $D \times H' \times W'$  is the spatial resolution discretizing the 3D space. The 3D heatmap encodes per-voxel likelihood of containing each robot keypoint. We derive the root-relative 3D positions of each keypoint  $\mathbf{P}_n^r$  by performing spatial integral techniques [33] over the corresponding heatmap  $\mathbf{H}_n$  in a differentiable manner:

$$\mathbf{P}_n^r = \sum_{k=1}^D \sum_{i=1}^{H'} \sum_{j=1}^{W'} (k, i, j) \cdot \mathbf{H}_n(k, i, j). \quad (3)$$

By combining  $\mathbf{P}^r$  with the estimated root depth  $d$ , we obtain the regressed 3D keypoint locations  $\mathbf{P}'$  and root translation  $\mathbf{t}$ . We further calculate the FK-based 3D keypoint locations  $\mathbf{P}$  with differentiable FK parameterized by  $\mathbf{q}$ ,  $\mathbf{R}$ , and  $\mathbf{t}$ .

### 3.3. Training loss

#### 3.3.1 Ground-truth supervision

For training on synthetic datasets where we have access to all the ground-truth information, we apply separate supervision for all the sub-tasks to train the corresponding network modules:

$$\mathcal{L}_{\text{depth}} = \|d - \hat{d}\|_1, \quad (4)$$

$$\mathcal{L}_{\text{joint}} = \|\mathbf{q} - \hat{\mathbf{q}}\|_2, \quad (5)$$

$$\mathcal{L}_{\text{rot}} = \|\mathbf{R} - \hat{\mathbf{R}}\|_2, \quad (6)$$

$$\mathcal{L}_{\text{trans}} = \|\mathbf{t} - \hat{\mathbf{t}}\|_2, \quad (7)$$



$$\mathcal{L}_{\text{kpts}} = \|\mathbf{P} - \hat{\mathbf{P}}\|_2 + \|\mathbf{p} - \hat{\mathbf{p}}\|_2, \quad (8)$$

$$\mathcal{L}'_{\text{kpts}} = \|\mathbf{P}' - \hat{\mathbf{P}}'\|_2 + \|\mathbf{p}' - \hat{\mathbf{p}}'\|_2, \quad (9)$$

where  $d$ ,  $\mathbf{q}$ ,  $\mathbf{R}$ ,  $\mathbf{t}$ ,  $\mathbf{P}$ , and  $\mathbf{P}'$  are GT root depth, joint states, camera-to-robot rotation and translation, FK-based keypoint locations and regressed keypoint locations, respectively;  $\mathbf{p}$  and  $\mathbf{p}'$  are 2D projections of  $\mathbf{P}$  and  $\mathbf{P}'$  using the camera intrinsics;  $\hat{\cdot}$  denotes model estimations.

We then train all the network modules end-to-end using

$$\mathcal{L}_{\text{GT}} = \mathcal{L}_{\text{joint}} + \mathcal{L}_{\text{rot}} + \mathcal{L}_{\text{trans}} + \lambda(\mathcal{L}_{\text{kpts}} + \mathcal{L}'_{\text{kpts}}). \quad (10)$$

where we set  $\lambda = 10.0$  to balance the loss terms.

### 3.3.2 Self-supervision

Apart from GT supervision on synthetic data, our framework also enables scaling the training pipeline to unlabeled real-world data in a self-supervised manner [21]. We employ two consistency-based training regularizations to improve model generalization.

Despite the absence of GT robot state parameters and keypoint locations, we regularize the consistency of the FK-based 3D keypoints  $\hat{\mathbf{P}}$  and regressed 3D keypoints  $\mathbf{P}'$  by:

$$\mathcal{L}_{\text{kc}} = \|\hat{\mathbf{P}} - \mathbf{P}'\|_2. \quad (11)$$

The keypoint consistency regularization effectively reconciles the predictions subject to robot structure constraints  $\hat{\mathbf{P}}$  and predictions based on the pixel-aligned feature  $\mathbf{P}'$ .

In addition, we also regularize the consistency between robot rendering mask  $\mathbf{M}_{\text{render}}$  and foreground segmentation mask  $\mathbf{M}_{\text{seg}}$  using their Intersection-over-Union (IoU):

$$\mathcal{L}_{\text{mc}} = 1 - \frac{\mathcal{S}_{\text{intersection}}}{\mathcal{S}_{\text{union}}}, \quad (12)$$

where  $\mathcal{S}_{\text{intersection}}$  and  $\mathcal{S}_{\text{union}}$  is the area of the intersection and the union of  $\mathbf{M}_{\text{render}}$  and  $\mathbf{M}_{\text{seg}}$ , respectively.  $\mathbf{M}_{\text{render}}$  is obtained with differentiable rendering using  $\mathbf{q}$ ,  $\mathbf{R}$ , and  $\mathbf{t}$  [14];  $\mathbf{M}_{\text{seg}}$  is obtained with an image segmentation model [21].

The overall self-supervision training objective is as follows:

$$\mathcal{L}_{\text{self}} = \mathcal{L}_{\text{kc}} + \lambda_{\text{mc}} \mathcal{L}_{\text{mc}} \quad (13)$$

where we set  $\lambda_{\text{mc}} = 1.0$ . We apply end-to-end self-supervised training for the sim-to-real domain adaptation stage.

## 4. Experiments

### 4.1. Dataset and metrics

We utilize the benchmark dataset DREAM [17], for both training and testing in our study. This dataset comprises images from three widely used robotic arms, namely, Franka Emika Panda, Kuka iiwa7, and Rethink Robotics Baxter. The training dataset for each robot consists of approximately 100k synthetic images generated using the domain randomization (DR) technique. These images encompass scenarios with varying camera-to-robot poses and joint states. The testing datasets include both DR-generated synthetic images for each robot and photorealistic synthetic images (denoted as "Photo") for the Panda and Kuka robots.

Additionally, real-world image datasets of Panda are provided. Panda-3Cam comprises a total of 17k image frames captured by three different cameras, namely Azure Kinect (AK), XBOX 360 Kinect (XK), and Realsense (RS). This dataset is presented as three sub-datasets, each corresponding to one camera. Another real-world dataset, Panda-ORB, contains 32,315 images captured from 27 viewpoints using a Realsense camera.

We evaluate the accuracy of our estimations using the Average Distance (ADD) metric, which represents the average Euclidean distances (in millimeters) between predicted 3D keypoint locations and their corresponding ground truth locations. Our reported metrics include both the Area Under the Curve (AUC) value and the mean value of ADD. The AUC integrates ADD over different thresholds, while the mean value effectively represents the general prediction accuracy.

### 4.2. Implementation details

We first pre-train *DepthNet* on the synthetic training dataset for 100 epochs, employing a learning rate of  $1e-4$  and relying solely on ground truth supervision for depth. Subsequently, we conduct training for our entire model based on the pretrained *DepthNet* for an additional 100 epochs with a learning rate of  $1e-4$  and a decay rate of 0.95. The Adam optimizer is employed in each stage to optimize the network parameters, with the momentum set to 0.9. As depth influences the global offset of all keypoints, a pre-trained *DepthNet* serves as a reasonable starting point for training other networks. On the Panda real datasets, we further apply self-supervised training on real-world images to overcome the sim-to-real domain gap. A learning rate of  $1e-6$  is applied. This fine-tuning process uses only image data and no ground-truth labels.

### 4.3. Evaluation and Comparison

#### 4.3.1 Accuracy

We first quantitatively evaluate the estimation accuracy of our method and compare it with the state-of-the-art (SOTA) ap-

| Method         | Baxter DR   | Kuka DR     | Kuka Photo  | Panda DR    | Panda Photo | Panda 3CAM-AK | Panda 3CAM-XK | Panda 3CAM-RS | Panda ORB   |
|----------------|-------------|-------------|-------------|-------------|-------------|---------------|---------------|---------------|-------------|
| † DREAM-F [17] | -           | -           | -           | 81.3        | 79.5        | 68.9          | 24.4          | 76.1          | 61.9        |
| † DREAM-Q [17] | 75.5        | -           | -           | 77.8        | 74.3        | 52.4          | 37.5          | 78.0          | 57.1        |
| † DREAM-H [17] | -           | 73.3        | 72.1        | 82.9        | 81.1        | 60.5          | 64.0          | 78.8          | 69.1        |
| RoboPose [14]  | 32.7        | <b>80.2</b> | 73.2        | <b>82.9</b> | 79.7        | 70.4          | <b>77.6</b>   | 74.3          | 70.4        |
| Ours           | <b>58.8</b> | 75.1        | <b>73.9</b> | 82.7        | <b>82.0</b> | <b>82.2</b>   | 76.0          | <b>75.2</b>   | <b>75.2</b> |

Table 1. Comparison of AUC  $\uparrow$  of the ADD distribution curve on each dataset on the DREAM datasets. Panda 3CAM datasets and Panda ORB are real-world datasets and the rest are synthetic datasets. † denotes using ground-truth joint state parameters.

| Method         | Baxter DR   | Kuka DR     | Kuka Photo  | Panda DR    | Panda Photo | Panda 3CAM-AK | Panda 3CAM-XK | Panda 3CAM-RS | Panda ORB   |
|----------------|-------------|-------------|-------------|-------------|-------------|---------------|---------------|---------------|-------------|
| † DREAM-F [17] | -           | -           | -           | 552.0       | 785.8       | 11413.1       | 491911.4      | 2077.4        | 95319.1     |
| † DREAM-Q [17] | 59.0        | -           | -           | 359.0       | 569.0       | 78089.3       | 54178.2       | 27.2          | 64247.6     |
| † DREAM-H [17] | -           | 5613.2      | 11099.4     | 325.6       | 518.8       | 56.5          | 7381.6        | 23.6          | 25685.3     |
| RoboPose [14]  | 87.9        | 34.2        | 89.0        | 21.4        | 32.2        | 34.3          | <b>22.3</b>   | 26.0          | 30.1        |
| Ours           | <b>45.0</b> | <b>28.0</b> | <b>29.0</b> | <b>18.0</b> | <b>18.4</b> | <b>18.9</b>   | 24.0          | <b>24.8</b>   | <b>24.8</b> |

Table 2. Comparison of mean  $\downarrow$  of the ADD (mm) on the DREAM datasets. † denotes using ground-truth joint state parameters.

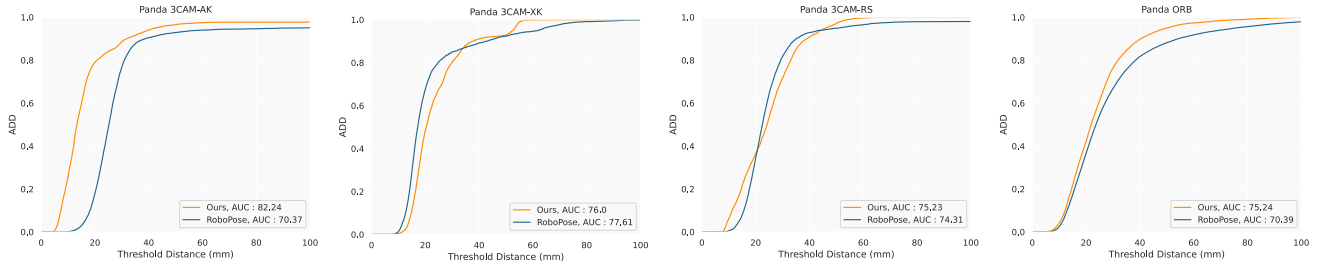


Figure 3. Comparison of ADD distributions on the real-world datasets between our approach and RoboPose [14].

proaches. To the best of our knowledge, only RoboPose [14] addresses a scenario similar to ours, where both the pose and joint state parameters for an industry-level robot are estimated from a single RGB image. We also present the results of DREAM [17], a representative feed-forward method using ground-truth joint state parameters, as a reference.

Tabs. 1 and 2 present the comparisons of AUC and the mean value of ADD. Our method outperforms SOTA on most datasets, significantly reducing joint localization errors. Specifically, DREAM [17] detects the 2D keypoint locations first, then employs a PnP process to solve the 2D-to-3D transformation. However, once the 2D keypoint detector fails due to truncations and occlusions, the PnP process produces unreliable numerical solutions. RoboPose [14] utilizes iterative render-and-compare, which is prone to falling into local optima on complex robot models with symmetric structures (e.g., Baxter). In contrast, our approach directly regresses both the robot pose and joint state parameters, enabling end-to-end optimization from multi-facet supervision signals. We also visualize the complete ADD distribution. As shown in Fig. 3, our approach achieves higher accuracy across most ADD thresholds. Notably, our approach attains near 100%

| Method         | AUC $\uparrow$ | Time (ms) $\downarrow$ | FPS $\uparrow$ | FLOPS (G) $\downarrow$ |
|----------------|----------------|------------------------|----------------|------------------------|
| † DREAM-F [17] | 68.9           | 66.0                   | 15.1           | 90.5                   |
| RoboPose [14]  | 70.4           | 570.8                  | 1.8            | 57.3                   |
| Ours           | <b>82.2</b>    | <b>44.3</b>            | <b>22.6</b>    | <b>25.2</b>            |

Table 3. Comparison of computation efficiency on the Panda 3CAM-AK dataset. † denotes using ground-truth joint state parameters.

accuracy with a 60mm threshold, indicating more reliable estimation results on challenging cases with fewer outliers, as demonstrated below in the qualitative comparisons.

Finally, we visualize the predictions of our approach and compare them with SOTA to better understand the performance improvement. Figure 4 illustrates our approach’s ability to produce high-quality estimates across different robot morphologies. Particularly, our approach demonstrates superior performance in highly challenging cases, including self-occlusions, truncations, and extreme lighting conditions.

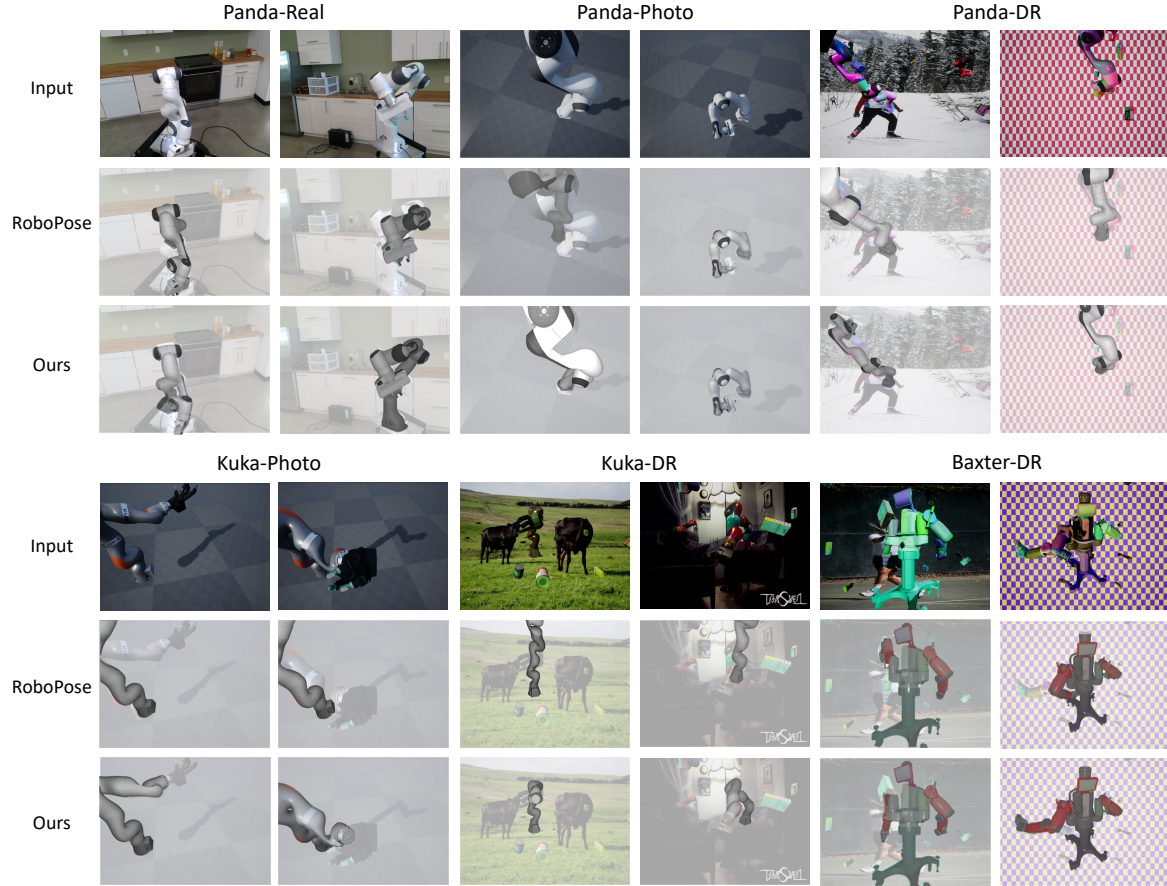


Figure 4. Qualitative comparison between our method and RoboPose [14] on both real and synthetic datasets.

### 4.3.2 Efficiency

Furthermore, we benchmark the computation efficiency of our method and compare it with previous works. We measure the average inference time, frame per second (FPS), and Floating Point Operations (FLOPs). For a fair comparison, we benchmark all methods on a Linux machine with CPU Intel(R) Xeon(R) Gold 6240 CPU @ 2.60GHz and GPU NVIDIA Tesla V100S. Batch size is set to be 1 for all methods. Table 3 shows that our method exhibits a remarkable advantage in terms of inference speed and computation loads, enabling real-time inference while achieving state-of-the-art accuracy. This advantage stems from the fact that our method involves only a single feed-forward pass without costly iterative optimization during inference. We demonstrate that our approach serves as an efficient and effective solution for real-time holistic robot pose estimation, which holds great potential in real-world applications.

### 4.4. Comparison under known joints states

Although the primary focus of this work is holistic robot pose estimation with unknown states, our approach can also be

easily adapted to the known joint states setting. We conduct additional experiments on four real datasets for robot pose estimation with ground-truth joint states available. We simply replace the predicted joint state with the ground-truth joint state during the self-supervised training process. As shown in Tabs. 4 and 5, our approach also achieves comparable performance with previous SOTA under this well-explored setting.

## 4.5. Ablation study

### 4.5.1 Ablation on network modules

We first conduct an ablation study on the proposed network modules to investigate their effectiveness. Since *JointNet* and *RotationNet* are the major regression targets of our task, we focus on the ablation of two assistive network modules, *DepthNet* and *KeypointNet*. We conduct the experiments on the synthetic datasets, utilizing only ground-truth supervision to simplify the process.

Firstly, we delve into the implementation of *DepthNet*. In Tab. 6, we evaluate the design choice of whether to share the backbone of *DepthNet* with other modules or not. The

| Method        | Panda 3CAM-AK | Panda 3CAM-XK | Panda 3CAM-RS | Panda ORB   |
|---------------|---------------|---------------|---------------|-------------|
| DREAM-F [17]  | 68.9          | 24.4          | 76.1          | 61.9        |
| DREAM-Q [17]  | 52.4          | 37.5          | 78.0          | 57.1        |
| DREAM-H [17]  | 60.5          | 64.0          | 78.8          | 69.1        |
| RoboPose [14] | 76.5          | <b>86.0</b>   | 76.9          | 80.5        |
| CtRNet [21]   | 89.9          | 79.5          | 90.8          | 85.3        |
| SGTAPose [35] | 67.8          | 2.1           | 87.6          | 72.3        |
| Ours          | <b>90.2</b>   | 81.2          | <b>91.9</b>   | <b>87.6</b> |

Table 4. Comparison of AUC  $\uparrow$  of the ADD distribution curve on the real-world datasets of DREAM, with all methods using **known ground-truth joint state parameters**.

| Method        | Panda 3CAM-AK | Panda 3CAM-XK | Panda 3CAM-RS | Panda ORB   |
|---------------|---------------|---------------|---------------|-------------|
| DREAM-F [17]  | 11413.1       | 491911.4      | 2077.4        | 95319.1     |
| DREAM-Q [17]  | 78089.3       | 54178.2       | 27.2          | 64247.6     |
| DREAM-H [17]  | 56.5          | 7381.6        | 23.6          | 25685.3     |
| RoboPose [14] | 24.2          | <b>14.0</b>   | 23.1          | 19.4        |
| CtRNet [21]   | 13.0          | 32.0          | <b>10.0</b>   | 21.0        |
| SGTAPose [35] | 35.7          | 157.7         | 12.8          | 35.0        |
| Ours          | <b>12.9</b>   | 19.9          | 11.0          | <b>15.9</b> |

Table 5. Comparison of Mean  $\downarrow$  of the ADD (mm) on the real-world datasets of DREAM, with all methods using **known ground-truth joint state parameters**.

| Dataset         | Separate | AUC $\uparrow$ | Mean (mm) $\downarrow$ |
|-----------------|----------|----------------|------------------------|
| Panda DR (a)    | —        | 79.98          | 21.9                   |
| Panda DR (b)    | +        | <b>82.68</b>   | <b>18.0</b>            |
| Panda Photo (a) | —        | 79.66          | 22.0                   |
| Panda Photo (b) | +        | <b>81.98</b>   | <b>18.4</b>            |

Table 6. Ablation studies on the effect of separating *DepthNet* image feature extractor.

| Dataset         | Pretrain | AUC $\uparrow$ | Mean (mm) $\downarrow$ |
|-----------------|----------|----------------|------------------------|
| Panda DR (a)    | —        | 74.29          | 26.8                   |
| Panda DR (b)    | +        | <b>82.68</b>   | <b>18.0</b>            |
| Panda Photo (a) | —        | 73.34          | 27.9                   |
| Panda Photo (b) | +        | <b>81.98</b>   | <b>18.4</b>            |

Table 7. Ablation studies on the effect of pre-training *DepthNet*.

results indicate that separating the *DepthNet* backbone consistently improves performance. This improvement could be explained by the fact that *DepthNet* involves learning scale-variant features, while the other network modules all focus on learning scale-invariant features. We also investigate whether to pre-train the *DepthNet* or jointly train it with other modules from scratch. Table 7 suggests that a pre-training stage leads to considerable performance improvement. This improvement likely occurs because a well-trained *DepthNet* reliably aids other modules in better training, as it determines the global translation of all joints.

Moreover, we conduct ablation experiments to investigate the impact of *KeypointNet* on other network modules, namely *JointNet* and *RotationNet*. We utilize Mean Joint Error, which represents the mean error of the joint state parameter predictions, and the Mean Rotation Angle Error [14], which represents the mean error of the Euler angle predictions ( $\theta_x^{pred}$ ,  $\theta_y^{pred}$ ,  $\theta_z^{pred}$ ) for the camera-to-robot rotation,

to quantify the accuracy of the *JointNet* and *RotationNet* predictions, respectively. It is important to note that a Panda robot consists of seven revolute joints with angle parameters (representing one-DoF rotations) and one prismatic joint with a length parameter (representing one-DoF translation). Therefore, we calculate the Mean Joint Error separately for the revolute and prismatic joints. Tables 8 and 9 show that the presence of *KeypointNet* significantly improves the prediction accuracy of *JointNet* and *RotationNet*. By sharing a feature extractor with *JointNet* and *RotationNet*, *KeypointNet* guides the network towards learning pixel-aligned robot visual features, which further assists in estimating robot pose and joint states.

Finally, we examine the overall effect of *DepthNet* and *KeypointNet*. To replace *DepthNet*, we implement a straightforward alternative, directly regressing the camera-to-robot translation  $\mathbf{t}$  from image features  $\mathbf{f}$  using an MLP, similar to *RotationNet*. Figure 5 illustrates that both modules play an important role in prediction accuracy. The *DepthNet* notably



| Dataset              | KeypointNet | Mean Joint Error ↓ |
|----------------------|-------------|--------------------|
| Panda DR Joint1-7    | —           | 14.49°             |
| Panda DR Joint1-7    | +           | <b>9.29°</b>       |
| Panda Photo Joint1-7 | —           | 15.14°             |
| Panda Photo Joint1-7 | +           | <b>10.45°</b>      |
| Panda DR Joint8      | —           | 3.45 mm            |
| Panda DR Joint8      | +           | <b>2.63 mm</b>     |
| Panda Photo Joint8   | —           | 3.83 mm            |
| Panda Photo Joint8   | +           | <b>2.69 mm</b>     |
| Kuka DR              | —           | 9.59°              |
| Kuka DR              | +           | <b>8.25°</b>       |
| Kuka Photo           | —           | 9.51°              |
| Kuka Photo           | +           | <b>8.22°</b>       |
| Baxter DR            | —           | 13.73°             |
| Baxter DR            | +           | <b>12.95°</b>      |

Table 8. Ablation studies on the influence of *KeypointNet* on *JointNet*.

| Dataset     | KeypointNet | Mean Rotation Angle Error (°) ↓ |
|-------------|-------------|---------------------------------|
| Panda DR    | —           | 3.78                            |
| Panda DR    | +           | <b>3.25</b>                     |
| Panda Photo | —           | 4.03                            |
| Panda Photo | +           | <b>3.36</b>                     |
| Kuka DR     | —           | 8.14                            |
| Kuka DR     | +           | <b>7.12</b>                     |
| Kuka Photo  | —           | 8.28                            |
| Kuka Photo  | +           | <b>7.38</b>                     |
| Baxter DR   | —           | 4.36                            |
| Baxter DR   | +           | <b>3.69</b>                     |

Table 9. Ablation studies on the influence of *KeypointNet* on *RotationNet*.

enhances accuracy by improving root depth estimation, a global offset that affects the precision of all joints. Meanwhile, *KeypointNet* further benefits the estimation results.

The contribution of these modules to the overall performance validates our design. *DepthNet* disentangles depth from camera intrinsics, facilitating a learning-based approach to depth estimation. This method exhibits greater expressive capability compared to the analytical, non-parameterized PnP methods employed in previous work[17, 21, 35]. On the other hand, *KeypointNet* enhances both *JointNet* and *RotationNet* by steering the shared backbone towards learning more pixel-aligned features, thus complementing the learning objectives defined in the robot kinematic space.

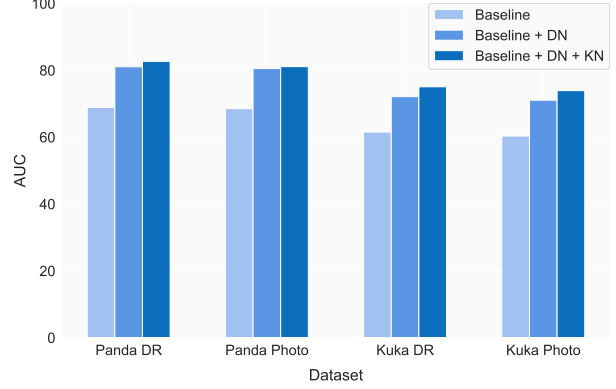


Figure 5. Ablation study on network modules. ‘Baseline’ represents direct regression, ‘DN’ and ‘KN’ refer to *DepthNet* and *KeypointNet*, respectively.

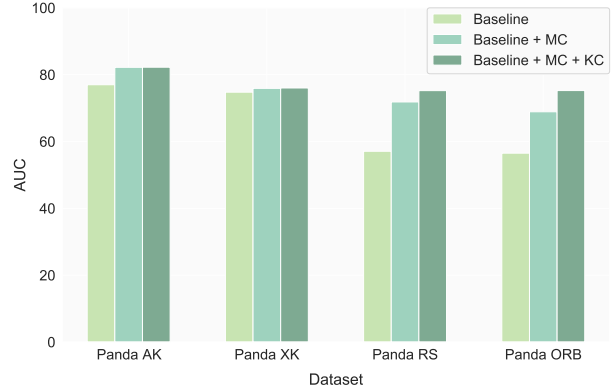


Figure 6. Ablation study on self-supervision. ‘Baseline’ represents no self-supervision, ‘MC’ and ‘KC’ refer to mask and keypoint consistency regularization, respectively.

#### 4.5.2 Ablation on self-supervision

We also perform an ablation study of our self-supervised learning objectives. We conduct the experiments on the Panda real datasets. Figure 6 demonstrates that both the keypoint consistency regularization and the mask consistency regularization contribute to the overall performance. Specifically, the mask consistency regularization provides pixel-wise supervision signal with the help of differentiable rendering, while the keypoint consistency regularization unifies the predictions in the pixel space and that in the robot kinematic space. We suppose that pixel-aligned 2D tasks, e.g. keypoint detection and mask segmentation, generally generalize better, and could therefore improve the 3D estimation quality through consistency regularization, further improving the overall performance.

## 5. Conclusion

This work presents a novel end-to-end framework for holistic robot pose estimation without prior knowledge of internal robot states. By decomposing this complex task into specific sub-tasks and tailoring neural network modules for each, the method efficiently addresses the challenges while retaining high computation efficiency. Our approach, which circumvents iterative optimization, significantly accelerates the estimation process and achieves state-of-the-art accuracy. This advancement holds promise for enhancing real-world applications in robotics, offering a practical solution for real-time robot pose estimation and state monitoring.

## References

- [1] Simon Bultmann, Raphael Memmesheimer, and Sven Behnke. External camera-based mobile robot pose estimation for collaborative perception with smart edge sensors. In *ICRA*, 2023. 1
- [2] Linghao Chen, Yuzhe Qin, Xiaowei Zhou, and Hao Su. Easy-HeC: Accurate and Automatic Hand-eye Calibration via Differentiable Rendering and Space Exploration. In *IEEE Robotics and Automation Letters*, 2023. 3
- [3] Sammy Christen, Wei Yang, Claudia Pérez-D’Arpino, Otmar Hilliges, Dieter Fox, and Yu-Wei Chao. Learning human-to-robot handovers from point clouds. In *Proceedings of the IEEE/CVF Conference on Computer Vision and Pattern Recognition*, pages 9654–9664, 2023. 1
- [4] Marc Peter Deisenroth, Carl Edward Rasmussen, and Dieter Fox. Learning to control a low-cost manipulator using data-efficient reinforcement learning. *Robotics: Science and Systems VII*, 7:57–64, 2011. 2
- [5] Ashley Feniello, Hao Nguyen Dang, and Stan Birchfield. Program synthesis by examples for object repositioning tasks. *2014 IEEE/RSJ International Conference on Intelligent Robots and Systems*, pages 4428–4435, 2014. 2
- [6] Mark Fiala. Artag, a fiducial marker system using digital techniques. In *CVPR*, 2005. 2
- [7] Sergio Garrido-Jurado, Rafael Muñoz-Salinas, Francisco José Madrid-Cuevas, and Manuel Jesús Marín-Jiménez. Automatic generation and detection of highly reliable fiducial markers under occlusion. *Pattern Recognition*, 2014. 2
- [8] Ran Hao, Orhan Özgüner, and M Cenk Çavuşoğlu. Vision-based surgical tool pose estimation for the da vinci® robotic surgical system. In *2018 IEEE/RSJ international conference on intelligent robots and systems (IROS)*, pages 1298–1305. IEEE, 2018. 3
- [9] Kaiming He, Xiangyu Zhang, Shaoqing Ren, and Jian Sun. Deep residual learning for image recognition. In *CVPR*, 2016. 1
- [10] Caglar Icli, Oleksandr Stepanenko, and Ilian Bonev. New method and portable measurement device for the calibration of industrial robots. *Sensors*, 20(20), 2020. 2
- [11] Bing Cai Kok and Harold Soh. Trust in robots: Challenges and opportunities. *Current Robotics Reports*, 1:297–309, 2020. 2
- [12] Nikunj Kothari, Misha Gupta, Leena Vachhani, and Hemendra Arya. Pose estimation for an autonomous vehicle using monocular vision. In *2017 Indian Control Conference (ICC)*, pages 424–431, 2017. 1
- [13] Benjamin Kuipers. How can we trust a robot? *Communications of the ACM*, 61(3):86–95, 2018. 2
- [14] Y. Labbé, J. Carpentier, M. Aubry, and J. Sivic. Single-view robot pose and joint angle estimation via render & compare. In *Proceedings of the Conference on Computer Vision and Pattern Recognition (CVPR)*, 2021. 1, 2, 3, 5, 6, 7, 8
- [15] Jens Lambrecht and Linh Kästner. Towards the usage of synthetic data for marker-less pose estimation of articulated robots in rgb images. In *ICAR*, 2019. 1
- [16] Jens Lambrecht, Philipp Grosenick, and Marvin Meusel. Optimizing keypoint-based single-shot camera-to-robot pose estimation through shape segmentation. In *2021 IEEE International Conference on Robotics and Automation (ICRA)*, pages 13843–13849. IEEE, 2021. 3
- [17] Timothy E Lee, Jonathan Tremblay, Thang To, Jia Cheng, Terry Mosier, Oliver Kroemer, Dieter Fox, and Stan Birchfield. Camera-to-robot pose estimation from a single image. In *International Conference on Robotics and Automation (ICRA)*, 2020. 1, 2, 3, 5, 6, 8, 9
- [18] Vincent Lepetit, Francesc Moreno-Noguer, and Pascal Fua. Epnp: An accurate o(n) solution to the pnp problem. *IJCV*, 2009. 3
- [19] Shushuai Li, Christophe De Wagter, and Guido CHE De Croon. Self-supervised monocular multi-robot relative localization with efficient deep neural networks. In *2022 International Conference on Robotics and Automation (ICRA)*, pages 9689–9695. IEEE, 2022. 1
- [20] Xiaohan Li, Xiaozhen Zhang, Xiang Zhou, and I-Ming Chen. Upg: 3d vision-based prediction framework for robotic grasping in multi-object scenes. *Knowledge-Based Systems*, 270: 110491, 2023. 1
- [21] Jingpei Lu, Florian Richter, and Michael C. Yip. Markerless camera-to-robot pose estimation via self-supervised sim-to-real transfer. In *Proceedings of the Conference on Computer Vision and Pattern Recognition (CVPR)*, 2023. 1, 2, 3, 5, 8, 9
- [22] Jeffrey Mahler, Matthew Matl, Vishal Satish, Michael Danielczuk, Bill DeRose, Stephen McKinley, and Ken Goldberg. Learning ambidextrous robot grasping policies. *Science Robotics*, 4(26):eaau4984, 2019. 2
- [23] Yue Ming, Xuyang Meng, Chunxiao Fan, and Hui Yu. Deep learning for monocular depth estimation: A review. *Neurocomputing*, 438:14–33, 2021. 4
- [24] Gyeongsik Moon, Juyong Chang, and Kyoung Mu Lee. Camera distance-aware top-down approach for 3d multi-person pose estimation from a single rgb image. In *The IEEE Conference on International Conference on Computer Vision (ICCV)*, 2019. 4
- [25] Douglas Morrison, Peter Corke, and Jürgen Leitner. Closing the Loop for Robotic Grasping: A Real-time, Generative Grasp Synthesis Approach. In *Proc. of Robotics: Science and Systems (RSS)*, 2018. 2
- [26] Edwin Olson. Apriltag: A robust and flexible visual fiducial system. In *ICRA*, 2011. 2
- [27] Andreas Papadimitriou, Sina Sharif Mansouri, and George Nikolakopoulos. Range-aided ego-centric collaborative pose estimation for multiple robots. *Expert Systems with Applications*, 202:117052, 2022. 1
- [28] Dongwon Park, Yonghyeok Seo, and Se Young Chun. Real-time, highly accurate robotic grasp detection using fully convolutional neural networks with high-resolution images, 2019. 2
- [29] Adam Paszke, Sam Gross, Soumith Chintala, Gregory Chanan, Edward Yang, Zachary DeVito, Zeming Lin, Alban Desmaison, Luca Antiga, and Adam Lerer. Automatic differentiation in pytorch. 2017. 1
- [30] A Prusak, O Melnychuk, H Roth, Ingo Schiller, and Reinhard Koch. Pose estimation and map building with a time-of-flight-camera for robot navigation. *International Journal of*

*Intelligent Systems Technologies and Applications*, 5(3-4): 355–364, 2008. 1

- [31] Arianna Rana, Fabio Vulpi, Rocco Galati, Annalisa Milella, and Antonio Petitti. A pose estimation algorithm for agricultural mobile robots using an rgb-d camera. In *2022 International Conference on Electrical, Computer, Communications and Mechatronics Engineering (ICECCME)*, pages 1–5, 2022. 1
- [32] Ke Sun, Bin Xiao, Dong Liu, and Jingdong Wang. Deep high-resolution representation learning for human pose estimation. In *CVPR*, 2019. 1
- [33] Xiao Sun, Bin Xiao, Fangyin Wei, Shuang Liang, and Yichen Wei. Integral human pose regression. In *Proceedings of the European Conference on Computer Vision (ECCV)*, 2018. 4
- [34] Mikael Svenstrup, Søren Tranberg, Hans Jørgen Andersen, and Thomas Bak. Pose estimation and adaptive robot behaviour for human-robot interaction. In *2009 IEEE International Conference on Robotics and Automation*, pages 3571–3576, 2009. 1
- [35] Yang Tian, Jiyao Zhang, Zekai Yin, and Hao Dong. Robot structure prior guided temporal attention for camera-to-robot pose estimation from image sequence. In *Proceedings of the Conference on Computer Vision and Pattern Recognition (CVPR)*, 2023. 1, 2, 3, 8, 9
- [36] Youya Xia, Yifan Tang, Yuhang Hu, and Guy Hoffman. Privacy-preserving pose estimation for human-robot interaction. *CoRR*, abs/2011.07387, 2020. 1
- [37] Chengjun Xu, Xinyi Yu, Zhengan Wang, and Linlin Ou. Multi-view human pose estimation in human-robot interaction. In *IECON 2020 The 46th Annual Conference of the IEEE Industrial Electronics Society*, pages 4769–4775, 2020. 1
- [38] Zhiren Xun, Jian Huang, Zhehan Li, Chao Xu, Fei Gao, and Yanjun Cao. Crepes: Cooperative relative pose estimation towards real-world multi-robot systems. *arXiv preprint arXiv:2302.01036*, 2023. 1
- [39] Wei Yang, Chris Paxton, Arsalan Mousavian, Yu-Wei Chao, Maya Cakmak, and Dieter Fox. Reactive human-to-robot handovers of arbitrary objects. In *IEEE International Conference on Robotics and Automation (ICRA)*. IEEE, 2021. 1
- [40] Yi Zhou, Connelly Barnes, Jingwan Lu, Jimei Yang, and Hao Li. On the continuity of rotation representations in neural networks. In *Proceedings of the IEEE/CVF Conference on Computer Vision and Pattern Recognition*, pages 5745–5753, 2019. 4
- [41] Yiming Zuo, Weichao Qiu, Lingxi Xie, Fangwei Zhong, Yizhou Wang, and Alan L Yuille. Craves: Controlling robotic arm with a vision-based economic system. In *CVPR*, 2019. 1, 2, 3



## Appendix

The content of our supplementary material is organized as follows.

1. Implementation details of our method.
2. Additional experiment results regarding the robot keypoints.
3. Error analysis of each sub-module across training stages.
4. Additional qualitative results of fresh-collected real-world laboratory images.
5. Failure cases of our method.

## S1. Implementation Details

### S1.1 Model architecture

We implement the proposed pipeline using PyTorch [29]. We utilize HRnet-w32 [32] as the feature extractor for *DepthNet*, *JointNet*, *RotationNet* and *KeypointNet* share a ResNet-50 [9] network as the feature extractor.

### S1.2 Robot arms

We leverage the datasets provided by DREAM [17], which contains images for three types of robot arms, namely Franka Emika Panda (Panda), Kuka iiwa7 (Kuka), and Rethink Robotics Baxter (Baxter).

Panda features 8 one-DoF joints and 7 keypoints, manually defined at joint articulations. The first 7 joints in Panda are revolute, facilitating pure rotational motion around a shared axis, and their internal state measures in degrees. The last joint is prismatic, allowing linear sliding along a shared axis without rotational motion, with its internal state measurable in millimeters.

Kuka comprises 7 one-DoF revolute joints and includes 8 defined keypoints. Baxter incorporates 15 one-DoF revolute joints and 17 defined keypoints. Both Kuka and Baxter have no prismatic joints.

Panda and Kuka are both single-arm robotic manipulators, while Baxter has multiple arms connected with a torso, resulting in a human-like appearance.

### S1.3 Rendering method

We utilize the provided Unified Robot Description Format (URDF) file following previous works [14, 21]. With URDF parsed and joint configuration  $\mathbf{q}$  given, we determine the robot’s morphology via forward kinematics, using the URDFPytorch module provided by [14].  $\mathbf{R}$  and  $\mathbf{t}$  determine the cam-to-robot-root transformation. As the robot’s own morphology and global pose are acquired, we render its mask with a given camera using a mesh renderer derived from [21].

## S2. Additional Experiment Results

### S2.1 Result with different number of in-frame keypoints

| Dataset       | In-frame KPs | Images | RoboPose [14]  |                   | Ours           |                   |
|---------------|--------------|--------|----------------|-------------------|----------------|-------------------|
|               |              |        | AUC $\uparrow$ | Mean $\downarrow$ | AUC $\uparrow$ | Mean $\downarrow$ |
| Panda 3CAM-AK | 4            | 96     | 52.28          | 47.71             | <b>62.54</b>   | <b>37.45</b>      |
| Panda 3CAM-AK | 5            | 92     | 73.88          | 26.11             | <b>79.31</b>   | <b>20.68</b>      |
| Panda 3CAM-AK | 6            | 105    | 6.05           | 126.87            | <b>71.98</b>   | <b>28.01</b>      |
| Panda 3CAM-AK | 7            | 6041   | 72.32          | 31.58             | <b>82.88</b>   | <b>18.29</b>      |
| Panda 3CAM-XK | 7            | 4966   | <b>77.61</b>   | <b>22.27</b>      | 76.01          | 23.99             |
| Panda 3CAM-RS | 5            | 100    | 38.60          | 61.39             | <b>76.57</b>   | <b>23.42</b>      |
| Panda 3CAM-RS | 6            | 11     | 35.83          | 64.16             | <b>74.56</b>   | <b>25.42</b>      |
| Panda 3CAM-RS | 7            | 5833   | 74.90          | 25.42             | <b>75.20</b>   | <b>24.79</b>      |
| Panda ORB     | 4            | 98     | <b>16.96</b>   | 88.73             | 14.40          | <b>85.66</b>      |
| Panda ORB     | 5            | 476    | 47.75          | 52.42             | <b>52.02</b>   | <b>47.97</b>      |
| Panda ORB     | 6            | 650    | 56.22          | 44.50             | <b>67.78</b>   | <b>32.21</b>      |
| Panda ORB     | 7            | 31091  | 71.20          | 29.28             | <b>75.94</b>   | <b>24.05</b>      |
| Panda Photo   | 2            | 4      | 36.05          | 186.04            | <b>38.57</b>   | <b>69.22</b>      |
| Panda Photo   | 3            | 17     | <b>53.44</b>   | 112.83            | 38.13          | <b>75.10</b>      |
| Panda Photo   | 4            | 491    | <b>66.65</b>   | 49.85             | 66.52          | <b>34.80</b>      |
| Panda Photo   | 5            | 207    | 74.06          | 36.89             | <b>76.74</b>   | <b>23.57</b>      |
| Panda Photo   | 6            | 202    | 73.80          | 43.72             | <b>78.43</b>   | <b>21.82</b>      |
| Panda Photo   | 7            | 5076   | <b>84.12</b>   | 24.76             | 84.01          | <b>16.21</b>      |
| Panda DR      | 2            | 4      | 0              | 17347.83          | <b>23.00</b>   | <b>77.40</b>      |
| Panda DR      | 3            | 10     | 0              | 15646.74          | <b>61.24</b>   | <b>38.75</b>      |
| Panda DR      | 4            | 391    | 52.19          | 58.09             | <b>68.04</b>   | <b>33.56</b>      |
| Panda DR      | 5            | 231    | 71.76          | 33.37             | <b>78.21</b>   | <b>21.83</b>      |
| Panda DR      | 6            | 206    | 78.16          | 25.66             | <b>79.59</b>   | <b>22.30</b>      |
| Panda DR      | 7            | 5156   | <b>86.02</b>   | 18.40             | 84.20          | <b>16.44</b>      |

Table 10. Performance comparison with different numbers of in-frame keypoints.

We observe that image truncation, *i.e.*, the partial capture of robot arms in images, considerably influences the estimation results. To evaluate our method’s robustness, we measure model performance with varying numbers of in-frame keypoints as detailed in Tab. 10. Our approach generally surpasses RoboPose [14] across various datasets and occlusion strengths, particularly in terms of mean estimation errors.

| Reference Root Keypoint | Mean Depth Error (mm) $\downarrow$ |
|-------------------------|------------------------------------|
| $\mathbf{P}_0$          | 18.07                              |
| $\mathbf{P}_1$          | 14.58                              |
| $\mathbf{P}_2$          | 13.00                              |
| $\mathbf{P}_3$          | <b>9.45</b>                        |
| $\mathbf{P}_4$          | 15.57                              |
| $\mathbf{P}_5$          | 18.13                              |
| $\mathbf{P}_6$          | 20.38                              |

Table 11. Ablation studies on the selection of reference root keypoint on the Panda DR dataset.

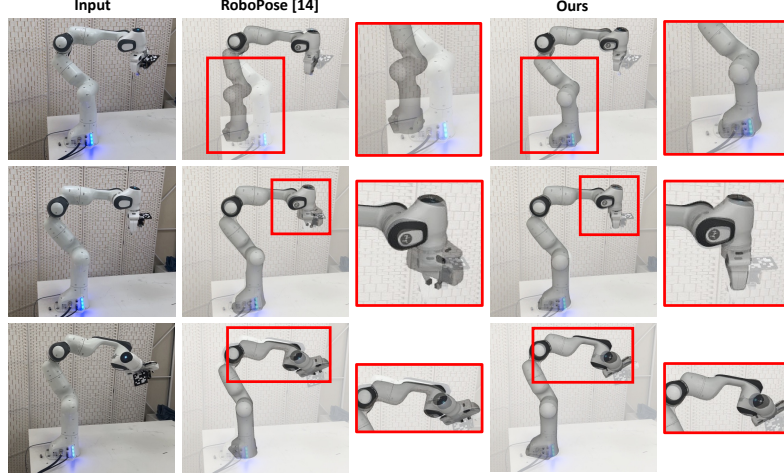


Figure 7. Additional qualitative results on in-the-wild images.

## S2.2 Results with different selection of robot root keypoint

In our experiments for all three robots, we designate the keypoint located in close proximity to the geometric center of the robot as the reference root keypoint. This choice is motivated by the observation that the keypoints near the geometric center are less likely to be truncated.

In addition, we quantitatively evaluate the selection of the reference root keypoint on the Panda DR dataset. We measure Mean Depth Error, which represents the mean error of the root depth predictions of *DepthNet*, under different reference root keypoints, denoted as  $\mathbf{P}_i (i \in 0, 1, 2, 3, 4, 5, 6)$ . Table 11 demonstrates that central keypoints indeed lead to more precise depth estimations, validating our choices.

## S3. Error Analysis

We further provide error analysis of each module across training stages (training on synthetic data and self-supervised training on real data) on Panda 3CAM-AK in Tab.12. The results show that our multi-stage training effectively reduces the errors, rather than accumulating them. Moreover, our end-to-end training could mitigate error propagation by jointly training all modules, allowing supervision signals to guide inter-module learning and prediction refinement. This contrasts with traditional RnC and non-differentiable PnP systems [14, 17], where error recovery is limited by the lack of integrated training.

## S4. Additional Qualitative Results

We present results on freshly-collected lab images in Fig. 7 (marker is not used). For example, in the image in the upper row, our method provides more accurate estimation of the pose of the robot’s base.

| Module      | Metric   | Synthetic | Self-supervised | Err. Change         |
|-------------|--|-----------|-----------------|---------------------|
| JointNet    | $\mathcal{L}_1$ Joint Angle Err. ( $^\circ$ )          | 9.68      | 8.83            | $\downarrow 8.8\%$  |
| RotationNet | $\mathcal{L}_1$ Euler Rotation Angle Err. ( $^\circ$ ) | 2.94      | 2.01            | $\downarrow 31.6\%$ |
| KeypointNet | Keypoint Euclidean Dis. (pixel)                        | 2.38      | 1.97            | $\downarrow 17.2\%$ |
| DepthNet    | $\mathcal{L}_1$ Root Depth Err. (mm)                   | 14.1      | 11.8            | $\downarrow 16.3\%$ |

Table 12. Error analysis of each module across training stages on Panda 3CAM-AK

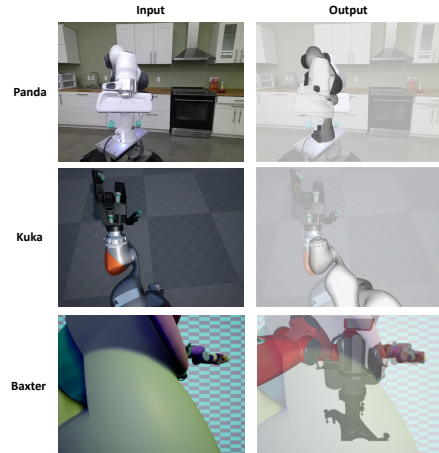


Figure 8. Typical failure cases.

## S5. Failure Cases

We illustrate the typical failure cases of our method for each robot arm in Fig. 8. In the case of Panda, estimation accuracy degrades under severe self-occlusion. For the example of Kuka and Baxter, estimating fails because of truncation. When only a small number of keypoints are in-frame, the estimations are generally more error-prone, as also evidenced in Tab. 10.